New insights on polar mesospheric cloud particle size distributions from a two-satellite common volume study

Journal of Atmospheric and Solar–Terrestrial Physics 219 (2021) 105594

Contents lists available at ScienceDirect

Journal of Atmospheric and Solar-Terrestrial Physics

journal homepage: www.elsevier.com/locate/jastp

New insights on polar mesospheric cloud particle size distributions from a two-satellite common volume study

Lina Broman [a,*], Jörg Gumbel [a], Ole Martin Christensen [a,b]

[a] Department of Meteorology, Stockholm University, Stockholm, Sweden
[b] Department of Earth and Space Sciences, Chalmers University of Technology, Gothenburg, Sweden

ARTICLE INFO

Keywords:
Polar mesospheric clouds
Size distribution
Common volume study
Remote sensing

ABSTRACT

The particle size distribution of Polar Mesospheric Clouds (PMC) is closely related to the fundamental processes of cloud formation and evolution. Still, despite substantial observational efforts, specific details about the particle size distribution have remained obscure. In this study, we aim at deriving more constraints on PMC size distributions by combining optical measurements from two satellite instruments observing a common PMC volume. We use a special set of 2D tomographic limb observations from the Optical Spectrograph and Infrared Imager System (OSIRIS) on the Odin satellite from 2010 to 2011 in the latitude range 78° N to 80° N and compare these to simultaneous PMC observations from the nadir-viewing Cloud Imaging and Particle Size (CIPS) instrument on the AIM satellite. A key goal is to find the assumption on the mathematical shape of the particle size distribution that should be applied to a vertically resolving limb-viewing instrument to reach consistent size results compared to the column-integrated ice distribution as seen by a nadir-viewing instrument. Our results demonstrate that viewing geometry and sampling volume of each instrument must be carefully considered and that the same size distribution assumption cannot simultaneously describe a column-integrated and a local height-resolved size distribution. In particular, applying the standard Gaussian assumption, used by many earlier PMC studies, to both limb and nadir observation leads to an overestimate of particle sizes seen by OSIRIS by about 10 nm as compared to CIPS. We show that the agreement can be improved if a Log-normal assumption with a broad distribution width around $\sigma = 1.42$ is adopted for OSIRIS. A reason for this broad distribution best describing the OSIRIS observations we suggest the large retrieval volume of the limb measurement. Gravity waves and other small-scale processes can cause horizontal variations and a co-existence of a wide range of particle populations in the sampling volume. Horizontal integration then leads to apparently much broader size distributions than encountered in a small horizontal sampling volume.

1. Introduction

The understanding of the Polar Mesospheric Cloud (PMC) particle size distribution has been developed in close synergy between various observational techniques and sophisticated numerical modeling, immensely increasing our insights in the complex dynamical and microphysical processes that affect the life cycle of the clouds (Rapp and Thomas, 2006; Merkel et al., 2009; Chandran et al., 2012; Wilms et al., 2016; Baumgarten et al., 2010). The PMC size distribution is directly linked to the physical processes such as nucleation, sedimentation and growth of ice particles. An accurate representation of all processes is essential for a correct description of the particle size distribution (PSD) in theoretical modeling and remote sensing studies. However, there is still an ongoing debate on which mathematical form best represents the size distributions of PMCs which ultimately leads to a large diversity of PMC particle size estimates among different instruments and measurement techniques.

PMCs have been extensively observed using optical instruments such as rockets, satellites and lidars that all possess the ability to provide PMC particle size estimates. Some of the very first studies of particle sizes were reported by Witt (1960) and Tozer and Beeson (1974), measuring linear polarization of scattered light from PMC using ground based observations and rocket experiments. These early findings indicated particle sizes smaller than 200 nm. The first particle size estimates from satellite experiments were reported by Thomas and McKay (1985) using data from Solar Mesosphere Explorer (Barth et al., 1983) satellite

* Corresponding author.
E-mail address: lina.broman@misu.su.se (L. Broman).

https://doi.org/10.1016/j.jastp.2021.105594
Received 1 December 2020; Received in revised form 8 February 2021; Accepted 15 February 2021
Available online 9 March 2021

measuring a combination of UV and visible light to derive color ratios of PMC scattering. Their findings suggested that the effective particle size is smaller than 70 nm. Since this pioneering work, several satellite instruments have provided size estimates of PMC e.g, SCIAMACHY on the ENVISAT satellite (Savigny and Burrows, 2007; Robert et al., 2009), the Optical Spectrograph and InfraRed Imager System (OSIRIS) on the Odin satellite (Karlsson and Gumbel, 2005; Savigny et al., 2005), the Solar Occultation For Ice Experiment (SOFIE) on the AIM satellite (Hervig et al., 2009) using spectroscopy and the Cloud Imaging and Particle Size (CIPS) instrument also on the AIM satellite using phase function analysis (Bailey et al., 2015b). Still, efforts to compare the particle sizes from these experiments have shown that the estimated particle sizes are not fully consistent. One reason for this is that the size information available from satellite-borne optical measurements is rather limited. None of the listed instruments possess the ability to measure the complete size distribution parameters of PMCs directly, but often only a single variable describing the size distribution can be derived. Often, this variable is chosen to be the mode radius, while several assumptions regarding other parameters of the size distribution (i.e the mathematical shape of the distribution and the width) are necessary for different remote sensing techniques. The limited information in the optical signal for size estimates is a problem that inherently makes it hard to compare size results from different instruments.

The assumption on the particle size distribution has been studied both using observations and models. Since pioneering work by Thomas and McKay (1985) and Cossart et al. (1999) the Log-normal assumption was used. It is described mathematically as

$$f(r) = \frac{1}{\sqrt{2\pi} r \ln(\sigma)} e^{\frac{-\left(\ln^2(r-r_m)\right)}{2\ln^2(\sigma)}} \quad (1)$$

with r_m being the median radius and σ the dimensionless width parameter. Thomas and McKay (1985) used both mono-disperse assumptions and Log-normal assumptions and adopted various distribution widths ranging from 1.0 to 2.0 in their work while Cossart et al. (1999) estimated σ to be 1.42 ± 0.22. However, the Log-normal assumption was later challenged by systematic analysis of large number of lidar measurements and model studies. Rapp and Thomas (2006) used the CARMA model to investigate PMC microphysics and suggested that a Gaussian distribution most closely describes the modeled ice particle size distribution, and that the Log-normal distribution leads to an overestimate of large particles and therefore should not be used for PMC size estimates. The Gaussian particle size distribution is described mathematically as

$$f(r) = \frac{1}{s\sqrt{2\pi}} e^{-\frac{1}{2}\left(\frac{r-r_m}{s}\right)^2} \quad (2)$$

where r_m denotes the mode radius, and s is the width. Currently, most instruments have adopted the Gaussian assumption to interpret the data (Baumgarten and Fritts, 2014; Lumpe et al., 2013). In recent years, many studies have additionally adopted a parametrization of the Gaussian distribution width as a function of mode radius based on comprehensive lidar analysis by Baumgarten et al. (2010), namely that the Gaussian width parameter is approximately $0.39 \times r_m$ for particle sizes up to 40 nm and stays fixed at 15.8 nm for larger particles. This Gaussian width - mean radius relationship will in the following be referred to only as the standard Gaussian assumption. Efforts to compare particle sizes from lidar and satellite instruments statistically have been presented by the Particle Size Workshop Group (Bailey et al., 2015a). By combining PMC particle size estimates from several instruments their findings show that a large discrepancy exists between particle sizes, sometimes of a factor 2, if the standard Gaussian assumption is adopted by all instruments, and that a Log-normal assumption is better suited to bring the size results from different instruments into agreement. Their findings also suggest that it is still not clear how the size distribution assumption is affected by instrument geometry, instrument sensitivity, integration time and observation volume, which suggests that the assumption on the mathematical shape of the particle size distribution is still not well constrained.

New approaches that combine the strength of different remote sensing instruments provide opportunities to explore the size distribution in greater detail. Bailey et al. (2015b) recently used a common volume approach to compare PMC properties from the two remote sensing instruments CIPS and SOFIE mounted on the AIM satellite. CIPS adopts nadir view of UV scattering and phase function analysis, and SOFIE adopts limb view and Visible/IR extinction through solar occultation. They showed that if the standard Gaussian assumption is used by both instruments, CIPS reports larger particle sizes than SOFIE. However, by assuming either a Log-normal with fixed width parameter of 1.52 or an Exponential distribution, the agreement between the instruments are improved.

In Broman et al. (2019), hereafter only referred to as BR19, we presented a method to compare PMC albedo and ice water content (IWC) from two instruments mounted on different satellites and adopting different viewing geometry. The approach took into account differences in viewing geometry and sensitivities, similar to the study by Bailey et al. (2015b). Using a common volume approach, we showed that CIPS PMC albedo and IWC and OSIRIS tomography PMC volume scattering coefficient and ice mass density can be made into comparable quantities in a common volume, and that these quantities agree within the specified errors of each instrument. In the current work, we extend our previous study between CIPS and OSIRIS and focus on particle sizes and especially the effect of the assumed shape of the size distribution using the most recent CIPS PMC data version 5.20.

OSIRIS (Llewellyn et al., 2004) on the Odin satellite (Murtagh et al., 2002) launched in February 2001 provides nearly global coverage of vertical profiles of middle atmosphere trace gases and ice layers. After careful separation of the molecular Rayleigh background radiation, PMCs can be detected as enhancements of limb scattered sunlight, and through the wavelength dependence of scattering OSIRIS provides particle size information. The vertically resolved PMC observations have previously been used to study the vertical variation of particle sizes (Savigny et al., 2005), thus experimentally confirming the sedimentation process. The OSIRIS PMC observations have also been used for studies of the interaction between the background atmosphere and the clouds (Christensen et al., 2016).

The nadir viewing CIPS instrument (Rusch et al., 2009) on the Aeronomy of Ice in the Mesosphere (AIM) spacecraft (Russell et al., 2009) launched in April 2007 images the PMCs over the polar caps in a very high horizontal resolution. The spacecraft was uniquely designed to provide deeper understanding of the processes that control PMC formation and lifetime as well as variation over time. CIPS measures in the UV, and provides particle size estimates from the angular variation of scattering. Since the launch of AIM, the morphology of the clouds has been explored and described in great detail (Thurairajah et al., 2013, 2017). Additionally, the effect of small scale dynamics (Gao et al., 2018; Rusch et al., 2017) as well as large scale waves (France et al., 2018; Bardeen et al., 2010) has been studied leading to deeper insight into the processes that affect cloud life cycle.

As in BR19, we use the OSIRIS tomographic PMC data where the retrieved PMC properties are presented on a horizontal-vertical plane. The horizontal axis is in the direction of the orbit, and vertical axis is the geometric altitude (in contrast to the non-tomographic OSIRIS PMC limb data that are retrieved as function of tangent altitude). The tomographic data have a high vertical resolution of 500 m and can therefore be used to study vertical cloud structures and vertical variation of microphysical properties in detail. The horizontal resolution of OSIRIS tomography is coarser in comparison. The horizontal extent of the grid cells is 56 km in the direction along the orbit and 30 km across the orbit track. CIPS observes the column integrated cloud properties at a very high spatial resolution. In the most recent CIPS PMC version 5.20, the resolution of

the pixels is 7.5 km × 7.5 km in the nadir. By combining two instruments that both measure in the UV and observe the same cloud volume but adopt very different measurement techniques, we have a favourable setup to study and constrain the assumption of the particle size distribution, which is the key goal of this study.

In Section 2 we present the datasets and discuss the size retrievals from each instrument. The method used to compare the cloud properties in the common volume is presented in Section 3. In Section 4 we present and discuss the results from the nominal particle size estimates from each instrument followed by a section where particle sizes are compared under different assumptions on the underlying particle size distribution for OSIRIS. Section 5 provides a summary of our findings.

2. Data

2.1. OSIRIS tomography particle size retrievals

Odin traverses a sun-synchronous polar orbit at around 600 km with ascending node at 18:00 local time. The orbit period is 96 min, allowing the satellite to complete 15 full orbits each day. The OSIRIS spectrograph, hereafter referred to only as OSIRIS, performs spectral measurements in a broad spectral range of 280–800 nm with about 1 nm spectral resolution. In the current study we use OSIRIS PMC measurements taken under a special tomographic mode under which the satellite was operated to only scan the mesosphere. The more narrow vertical span of the atmosphere in the tomographic mode allows for a larger set of lines of sight through the PMC layer, and enough information is sampled to invert the cloud signal using a tomographic inversion technique. The tomographic technique utilized by OSIRIS is based on multiplicative algebraic reconstruction technique (Lloyd and Llewellyn, 1989) and has been adapted to OSIRIS by Degenstein (1999) and Degenstein et al. (2003, 2004). The tomographic retrieval algorithm together with an error description was described in detail by Hultgren et al. (2013) and Hultgren and Gumbel (2014). The grid resolution of the tomographic retrieval is 0.5° × 500 m (Angle along orbit × altitude), where the Angle along orbit denotes the position of the OSIRIS tangent point along the satellite orbit, starting from 0° at equator crossing and increasing to 90°at the northmost position etc. The vertical extent of the tomographic dataset ranges from 76 km to 90 km, and the latitude range is confined to above about 50° N. The tomographic data have previously been compared to model simulations by Megner et al. (2016) and validated by a comparison to CIPS by BR19. In the following section we will briefly discuss OSIRIS tomography retrieval with focus on the retrieval of particle sizes, and the reader is referred to the above papers for in depth information.

The tomographic algorithm transforms the limb-integrated input radiance into an estimate of local volume scattering coefficient β_λ. It provides the ratio of the radiance scattered by the PMC to the solar irradiance and is expressed in unit [nm^{-1} sr^{-1}] in each grid cell for seven selected UV wavelengths (277.3, 283.5, 287.8, 291.2, 294.4, 300.2, 304.3 nm) These short wavelengths are chosen to utilize absorption by the stratospheric ozone layer, thus avoiding complications due to upwelling radiation from the lower atmosphere (Karlsson and Gumbel, 2005). Equation (3) relates the volume scattering coefficient to the microphysical properties of the PMC particle size distribution.

$$\beta_\lambda = N \int f(r, r_m) \frac{\partial \sigma}{\partial \Omega}(r, \lambda) dr \tag{3}$$

where N is the total number density, $f(r, r_m)$ is the normalized size distribution and $\frac{\partial \sigma}{\partial \Omega}$ is the differential scattering cross section for the direction in question. The differential scattering cross section can be written as the product of an absolute cross section and a phase function as a function of radius, wavelength and scattering angle. In eq. (3), the dependence on the scattering angle is taken into account when obtaining the monodisperse differential scattering cross section from the Müller matrix formalism before carrying out the integration over any desired size distribution based on eq. (3).

PMC particles lie within the size range where the scattering can be described using the Mie formalism for spherical particles, or using e.g. the T-matrix approach by Mishchenko and Travis (1998) for nonspherical particles. Within the limited OSIRIS spectral range of 277.3–304.3 nm, the wavelength dependence of the scattering on particle size can be approximated by the $\lambda^{-\alpha}$ relation, where α is the size dependent Ångström parameter. The spectral structure provided in β_λ combined with assumptions on the underlying size distribution can thus through the Ångström exponent be related to a mean particle radius. This is done by comparing the retrieved Ångström exponent to tabulated scattering simulations. Once the scattering coefficient and particle radius have been inferred in each grid cell, the particle number density and ice mass density (IMD) can be retrieved from equation (3). In the nominal OSIRIS retrieval, the same assumptions are made regarding shape of the particles and shape of the ice particle size distribution as in several previous studies, namely that the particles are assumed to be oblate spheroids with an axial ratio of 2, and the standard Gaussian distribution is assumed for the size distribution.

2.2. Special OSIRIS retrievals for this study

One of the key goals of this paper is to study the effect of the assumption on the underlying size distribution in achieving agreement between the CIPS and OSIRIS particle sizes. To analyse this, we have reprocessed the tomographic dataset for several other assumptions than the standard Gaussian assumption, while the assumption on the shape of the particles (oblate spheroids) is kept constant. Bailey et al. (2015b) suggested that an exponential assumption or a Log-normal assumption improve the agreement between CIPS and SOFIE compared to the standard Gaussian assumption and better represent the range of mass-bearing particles. The Exponential particle size distribution is described mathematically as

$$f(r) = \frac{1}{r_m} e^{-r/r_m} \tag{4}$$

where r_m denotes the mode radius.

We have formed a set of 25 different assumptions based on these three distributions and different distribution widths to represent a range from narrow to wide Gaussian and Log-normal distributions. The set includes Log-normal assumptions, where σ has been varied from 1.05 to 1.7 in steps of 0.02–0.05. The set also includes the Gaussian assumption with a fixed width ranging from 1 nm to 30 nm in steps of 5 nm. Finally, we include the exponential assumption.

2.3. CIPS nadir PMC size retrievals

CIPS (McClintock et al., 2009; Carstens et al., 2013) consists of four UV imaging nadir cameras that measure scattered radiance centered at 265 nm. For the time period analyzed in this study, the four cameras have an overlapping field of view of 120° along the orbit track and 80° across the orbit track. The camera suite takes multiple exposures of the PMCs from different scattering angles at a cadence of 43 s, which when combined provide a measure of the clouds phase function. By scattering theory, the phase function enables retrieval of particle sizes (Bailey et al., 2009). The images are combined into about 15 orbit swaths per day where each swath is typically 900 km wide and 8000 km long. The data used in this study are the most recent CIPS level 2 version 5.20 PMC data products cloud albedo, Ice Water Content, Ice column density and the Gaussian mode radii. Lumpe et al. (2013) provides a detailed description of the version 4.20 algorithm, together with error analysis. Since 2016, CIPS has been operated in a new mode using fewer scattering angles and reduced image cadence, however for the years 2010 and 2011 which is analyzed in this paper, the instrument was still

operated in the pre-2016 mode using 6–7 scattering angles to constrain the phase function. From the phase function a mean particle size can be derived, given necessary assumptions on particle shape and mathematical form of the size distribution. The nominal retrieval makes the same assumptions as the nominal OSIRIS retrieval, namely that the particles are assumed to be oblate spheroids with an axial ratio of 2, and the shape of the ice particle size distribution can be represented by the standard Gaussian assumption. From albedo and particle radius, the ice column density, in units of cm^{-2} can be derived as $\mathrm{ICD} = \frac{A_{\mathrm{PMC}}}{\sigma(r_m)}$, where A_{PMC} is the cloud albedo at 90° scattering angle, and $\sigma(r_m)$ is the scattering coefficient at 90° scattering angle. Finally, the column ice mass can be derived as $\mathrm{IWC} = \mathrm{ICD} \times \mathrm{V} \times \rho$, where V is the volume per ice particle and ρ is ice density.

3. Method

3.1. Common volume observations

The method used to compare PMC albedo and IWC in a common volume approach together with a detailed error analysis was described in detail in BR19. In this section, we therefore only briefly describe the common volume method itself and describe the method for the extended analysis focusing on particle sizes in more detail. The days when the Odin satellite was operated in a tomographic mode have been chosen to provide optimal temporal coincidence between Odin and AIM. The orbits of OSIRIS (equator passage ∼ 6 local time) and CIPS (equator passage ∼ 12 local time) intercept at a latitude around 78–80°N. Due to orbital parameters, the orbit period is slightly different for the two satellites, ∼ 96 min for Odin and ∼ 95 min for AIM, which leads to a slowly varying difference in satellite passage times at 78–80°north. For this study, we have chosen a narrow coincidence criteria of 5 min to minimize the risk of background winds acting on the ice particles within the common volume during the observation time. In total, the satellites produce common volume observations within the stated time and space for 45 overpasses during three consecutive days each month during June, July and August when the satellites are in ascending node. In this latitude, the satellite orbits cross almost perpendicular, producing simultaneous common volume observations where the vertical-horizontal footprint of OSIRIS is situated within the horizontal image plane of CIPS. The domain of the CIPS and OSIRIS common volume is defined by the instruments' viewing geometry bounded by OSIRIS field of view across track at the tangent point of 30 km, OSIRIS′ vertical range of 76 km–90 km, and the width of CIPS' orbits strip of 900 km on average. Within the common volume, we define a smaller subset as a "common volume element" (CVE). The horizontal extent of the CVE is defined by the horizontal extent of one OSIRIS grid cell which is 56 km × 30 km. The vertical extent of the CVE is similarly defined by OSIRIS altitude range. For CIPS, the data in the CVE is defined as the CIPS pixels that fall within this horizontal area. Based on the resolution of CIPS v 5.20 of 7.5 km × 7.5 km in the nadir, the number of CIPS pixels in the overlapping region is ∼ 32. The reader is referred to Figs. 1 and 3 in BR19 for details.

3.2. Integrated/averaged cloud properties in the CV

As already outlined in BR19, the cloud properties from CIPS and OSIRIS can be made directly comparable in the CVE by horizontally averaging the cloud properties reported by CIPS and vertically integrating the cloud properties reported by OSIRIS if measures are taken to account for differences in scattering conditions, sensitivity and resolution.

In brief, BR19 showed that the albedo observed by OSIRIS and CIPS in the CVE, $A_{\mathrm{CVE,OSIRIS}}$ and $A_{\mathrm{CVE,CIPS}}$, is found by integrating the OSIRIS volume scattering coefficient over the vertical column

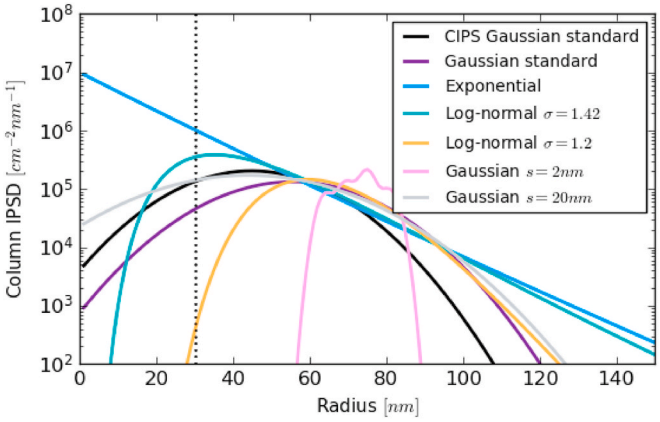

Fig. 1. Example total CVE size distributions. The black line shows CIPS size distribution, and the colored lines show the total size distribution for OSIRIS for six different assumptions. The dashed line marks the 30 nm size which is referred to in section 4.1.

$$A_{\mathrm{CVE,OSIRIS}} = \int_{76km}^{90km} \beta_{277nm} dz \tag{5}$$

where β_{277nm} is the derived volume scattering coefficient at 277 nm, and horizontally averaging the reported albedo in each CIPS pixel as

$$A_{\mathrm{CVE,CIPS}} = \frac{1}{k} \sum_{i=1}^{k} C_{phase} C_{spectral} A_{i,265nm}^{90^\circ} \tag{6}$$

C_{phase} and $C_{spectral}$ are conversion factors obtained from numerical T-matrix simulations (Mishchenko and Travis, 1998) that account for the difference in solar scattering angle and wavelengths between the instruments. We refer the reader to our previous study for details on the conversion factors. The summation over k describes an averaging over the common volume element for all CIPS pixels that are above the CIPS PMC detection threshold. Similarly, the IWC observed by OSIRIS and CIPS in the CVE, $\mathrm{IWC_{CVE,OSIRIS}}$ and $\mathrm{IWC_{CVE,CIPS}}$ respectively can be derived in the same way,

$$\mathrm{IWC_{CVE,OSIRIS}} = \int_{76km}^{90km} \mathrm{IMD} dz \tag{7}$$

and

$$\mathrm{IWC_{CVE,CIPS}} = \frac{1}{k} \sum_{i=1}^{k} \mathrm{IWC}_i \tag{8}$$

We now continue with a discussion on how we treat the size distribution assumption in the CVE and the different approaches to derive a mean particle radius for each instrument in the CVE. As already pointed out, a central idea of this paper is to compare particle sizes and size distributions in the common volume. Our approach is to base this on the established standard assumption on the size distribution for CIPS, while investigating various assumptions for OSIRIS. The Gaussian standard size distribution used in the retrieval of CIPS data products has been introduced in section 2.3. The Gaussian standard assumption is used to represent the size distribution of the particles in the vertical column of a CIPS retrieval pixel, and is here denoted as f_{CIPS} [nm^{-1}] in its normalized form. The size distribution assumed in the OSIRIS retrieval is denoted as f_{OS} [nm^{-1}] in its normalized form, and represents the size distribution of particles in a tomographic OSIRIS grid cell. The size distributions of both particle populations can also be expressed in absolute units, which we denote capital letters F_{CIPS} and F_{OS}. For each instrument, the size distribution in absolute units is formed by multiplying the normalized size distribution in each pixel/grid cell with the retrieved number density of

particles in each pixel/grid cell (ICD in units of cm^{-2} for CIPS and N in units of cm^{-3} for OSIRIS), $F_{CIPS} = ICD\, f_{CIPS}$ and $F_{OS} = N f_{OS}$. It is important to consider the size distribution of the total column particle population that each instrument observes in the larger CVE. For CIPS, this is obtained as the average over the size distribution over all CIPS pixels in the CVE as

$$F_{CVE,\ CIPS} = \frac{1}{k}\sum_{i=1}^{k} F^{i}_{CIPS} \tag{9}$$

where k is the number of cloudy CIPS pixels in the CVE. For OSIRIS, the corresponding CVE size distribution is obtained in terms of the height-integrated size distribution as

$$F_{CVE,OSIRIS} = \int_{76km}^{90km} F_{OS}\, dz \tag{10}$$

The corresponding normalized size distributions in CVE obtained from the CIPS and OSIRIS retrievals are denoted $f_{CVE,\ CIPS}$ and $f_{CVE,\ OSIRIS}$ respectively. These integrated/averaged size distributions, $F_{CVE,\ OSIRIS}$ and $F_{CVE,\ CIPS}$ will in the rest of the paper be referred to as total CVE size distribution for simplicity.

Fig. 1 shows one example of total CVE size distributions for CIPS and OSIRIS for a coincidence from CIPS orbit 17102 and OSIRIS orbit 50781 over 79° N and local time ~ 15. The total CVE size distribution from CIPS is shown by the black line and the colored lines show the total CVE size distribution for different size distribution assumptions in the OSIRIS retrieval. Note that each curve represents a summation over several distributions for each instrument, which is clearly evident from the strange shape of the Gaussian s = 2 nm curve. This results from the summation over discrete height intervals. A smooth curve could be expected if the vertical resolution of tomographic retrieval would be better than it is for OSIRIS.

Rather than comparing complete particle size distributions from CIPS and OSIRIS in the CVE, it can be convenient just to compare a specific particle size parameter, such as a *mean* radius or an *effective* radius. In principle, there exist several approaches to define a CVE mean radius depending on whether the purpose is a statistical study or a study of PMC microphysics. One can consider the non-weighted mean CVE particle size for OSIRIS and CIPS based on all grid cells/pixels where a radius is reported, (i.e, excluding faint cloud grid cells/pixels where a radius retrieval is impossible) and denote these r_{mean} as

$$r_{mean_{CVE,\ OSIRIS}} = \frac{1}{k}\sum_{i=1}^{k} r_{m,i} \tag{11}$$

where $r_{m,i}$ is the retrieved mean radius in each OSIRIS grid cell i and k is the number of vertical grid cells, and

$$r_{mean_{CVE,\ CIPS}} = \frac{1}{k}\sum_{i=1}^{k} r_{m,i} \tag{12}$$

where $r_{m,i}$ is the retrieved mean radius in each CIPS pixel i and k is the number of horizontal pixels. One can also consider a mean of the total CVE size distribution $f_{CVE,\ CIPS}$ or $f_{CVE,\ OSIRIS}$ as a more proper way of defining a CVE mean radius. This can be calculated as a weighted average of the mean particle size in the individual retrieval grid cells and pixels for each instrument as

$$r_{mean,N_{CVE,OSIRIS}} = \frac{\sum_{i=1}^{k} N_i r_{mean,i}}{\sum_{i=1}^{k} N_i} \tag{13}$$

and

$$r_{mean,N_{CVE,CIPS}} = \frac{\sum_{i=1}^{k} ICD_i r_{mean,i}}{\sum_{i=1}^{k} ICD_i} \tag{14}$$

Another approach is to compare the effective radius, r_{eff}, (Wyser, 1998; Merkel et al., 2009; Bailey et al., 2015b) defined by the ratio of the third moment of radius to the second moment as

$$r_{eff} = \frac{\int r^3 f(r) dr}{\int r^2 f(r) dr} \tag{15}$$

As compared to various mode radii connected to specific assumptions about size distributions, r_{eff} is a more universal measure of particle size, and is therefore an appealing particle property for comparison between different instruments. The effective radius is also, due to the numerator, sensitive to the bulk mass of the particles. We now define the CVE effective radius $r_{eff_{CV}}$ that each instrument observes based on the total CVE size distribution given in equations (9) and (10) as

$$r_{eff_{CVE,OSIRIS}} = \frac{\int r^3 f(r, r_m)_{CVE,OSIRIS} dr}{\int r^2 f(r, r_m)_{CVE,OSIRIS} dr} \tag{16}$$

$$r_{eff_{CVE,CIPS}} = \frac{\int r^3 f(r, r_m)_{CVE,CIPS} dr}{\int r^2 f(r, r_m)_{CVE,CIPS} dr} \tag{17}$$

4. Results and discussion

4.1. Comparison of nominal size estimates

Fig. 2 shows the agreement in CVE mean albedo between OSIRIS and CIPS for the nominal retrieval when the standard Gaussian assumption is adopted in both retrieval algorithms. Each point represents the observation in one CVE. The linear fit to the observations is shown by the black line and the line equation is given in the top of the figure together with the correlation coefficient r. The 1-to-1 relationship is shown by the dashed line. CVE albedo from the two instruments is in very good agreement with a correlation coefficient of 0.97. The observed mean difference between the instruments is only about 2 G ('G' is the fundamental CIPS albedo unit and corresponds to 10^{-6} sr^{-1}). This result is indeed expected since we showed already in BR19 that the agreement was excellent, based on the previous CIPS version (4.20). The result also confirms the robustness of the common volume analysis.

As will be further discussed in section 5, it is important to distinguish between *local* size distribution and *column* size distribution. The cloud formation is commonly described by a growth/sedimentation process (Rapp and Thomas, 2006). The initial formation is believed to occur through heterogeneous nucleation on meteoric smoke material (Gumbel

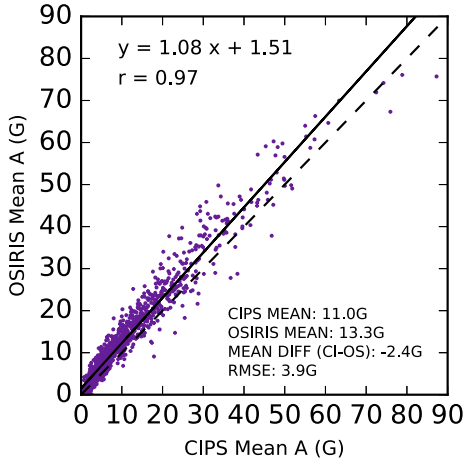

Fig. 2. Comparison of CIPS mean CVE albedo to OSIRIS mean CVE albedo. The notation 'G' corresponds to 10^{-6} sr^{-1}, and is the fundamental CIPS albedo unit. Both instruments adopt the standard Gaussian assumption for the size distribution. Each point represents one CVE observation. The linear fit to the data is shown by the black line, while the dashed line is the 1-to-1 line. The text information refers to all common volume observations in 2010–2011.

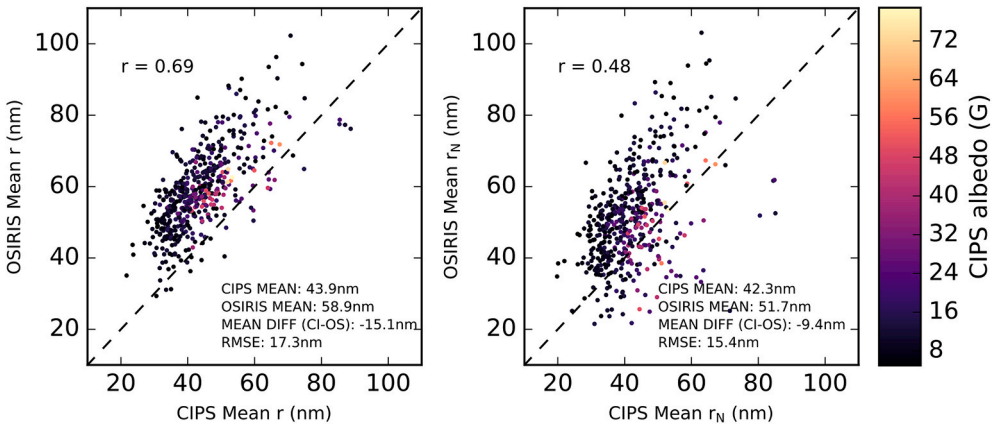

Fig. 3. Comparison of CIPS mean CVE particle radius to OSIRIS mean particle radius using the standard Gaussian assumption on the size distribution. The left panel shows the non-weighted mean CVE particle sizes calculated according to equations (11) and (12). In the right panel the mean sizes have been weighted by the number of particles in that grid according to equations (13) and (14). Each point represents one CVE observation. The text information refers to all common volume observations in 2010–2011.

and Megner, 2009) or possibly by condensation through amorphous solid water (Duft et al., 2019). The presence of meteoric smoke material in PMCs has been confirmed by satellite and rocket observations (Hervig et al., 2012; Antonsen et al., 2017). Nucleation of PMC particles starts near the mesopause in regions of high supersaturation. After formation, the nanometer sized particles slowly fall and grow by deposition of the surrounding water vapor (Zahn and Berger, 2003). Using trajectory models Kiliani et al. (2013) and Megner (2011) have demonstrated the importance of horizontal transport on the PMC growth. These studies show that the nucleation can occur in bursts, and that the particles can be transported for several days before rapid growth occurs only hours before the particles grow to visible sizes. As long as the particles are in a supersaturated region they can continue to grow to larger sizes before they eventually sediment out of the region and sublimate. If all ice particles were nucleated at the same altitude and then undergo the same growth/sedimentation process, one could expect to find only one particle size at a given altitude. In reality, nucleation happens over a certain altitude range, stochastic processes affect the microphysical growth, and turbulence mixes the particles. All this contributes to broadening the size distribution expected at a given altitude. However, for particles at a certain altitude (or at certain life stage) and over a limited horizontal extent, a rather narrow distribution can be expected. A size distribution representing the entire column of the cloud, on the other hand, could be expected to resemble the many phases of cloud evolution via the abundance of small ice particles in the top of the cloud to the region of fewer but large particles in the bottom of the cloud. In general, it cannot be expected that both a column distribution and a local distribution simultaneously can be described by the same assumptions about the mathematical shape etc. Nonetheless, the standard Gaussian assumption described in section 1 has been applied to both column and local PMC data. Therefore, in the following, we apply the assumption to analysis of both CIPS and OSIRIS, and we directly compare the resulting particle sizes derived from either data set.

Fig. 3 shows this comparison in mean CVE particle radius for the standard Gaussian assumption. We have restricted our analysis to good quality observations by excluding faint cloud volumes where the average observed albedo is below 2 G since the uncertainty in retrieved particle size is large for faint clouds. We additionally exclude the cloud volumes where the difference in observed average albedo exceeds 5 G since we do not expect agreement in particle sizes where albedo observations disagree. Finally, we have restricted the comparison to include only those CVE where CIPS reports a positive cloud detection and retrieved particle radius in at least 90 % of the pixels in the CVE. In the left panel the mean sizes are calculated according to equations (11) and (12), in the right panel the mean sizes are weighted by the number of particles in that grid according to equations (13) and (14). The mean radius as retrieved from OSIRIS is significantly larger than what is retrieved from CIPS for the same cloud volume for both averaging methods. The average over all 2010–2011 cloud volumes in the left panel yields a mean CVE radius of 58.9 nm for OSIRIS and 43.9 nm for CIPS, and similarly the mean over the whole CVE particle population in the right panel yields a mean CVE radius of 51.7 nm for OSIRIS and 42.3 nm for CIPS. The results clearly show that OSIRIS observes larger particles than CIPS if the same standard Gaussian assumption is adopted in both retrieval algorithms. The difference is about 10–15 nm, depending on averaging method.

The considerably large spread between the instruments, as given by a RMSE of 17.3 nm or 15.4 nm, indicates that even though the instruments observe very similar cloud brightness, the interpretation of scattered light in retrieving particle size using the retrieval algorithms clearly deviates and results in variegated size estimates. In most cases, the agreement is better for bright clouds than for faint clouds.

In Fig. 4 the distribution of mean radius is presented. Again, it can be seen that while using the standard Gaussian assumption for the size distribution, the range of mean CVE particle size is substantially larger for OSIRIS than CIPS, spanning from 20 nm to 100 nm while the majority of mean CV radii for CIPS falls in the range from 20 nm to 70 nm.

We conclude that even though the agreement in observed albedo generally is very good, the agreement in particle radius is only moderate. We argue that the reason can only be that the same assumption on the size distribution cannot simultaneously explain the range of particles observed both over a vertical column from a nadir-viewing instrument and in a narrow height interval as observed by a limb instrument. If we assume that the CIPS analysis uses the correct assumption on how the particles are distributed in vertical column, the same assumption cannot hold for the distribution seen by OSIRIS. In the next section we will

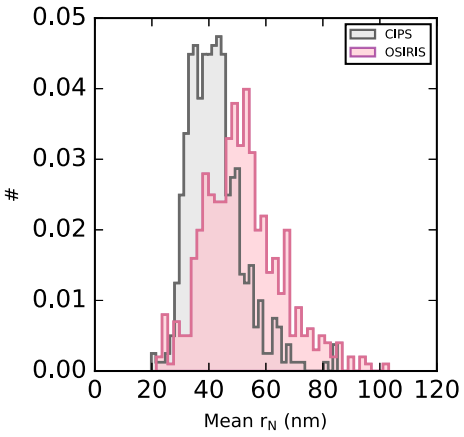

Fig. 4. Histogram of all observations of mean CVE radius from CIPS and OSIRIS. Same data points as in Fig. 3 (right). The number of CV observations is 491, and the number of bins is 40.

explore if the agreement between the instruments can be improved if the assumed size distribution is changed.

4.2. Comparison of size estimates for different PSD shape assumptions

We have re-processed OSIRIS tomography data using different assumptions on the underlying size distribution. We have then repeated the integration over the common volume element and the comparison to CIPS for the different assumptions. As specified in section 2.2, our study includes a set of 25 different assumptions based on the Gaussian, Log-normal and Exponential distributions. A direct comparison of a mean particle size is not meaningful when different assumptions are applied to both instruments. More relevant comparisons are based on the question of how the assumption on the size distribution affects the agreement between total CVE size distributions, effective radius and column ice content.

We argue that common volume studies of total CVE size distribution can be used to constrain the assumptions on the size distribution that best represent the limited particle size range seen by a vertically resolving limb instrument. The total CVE size distribution will naturally differ from one cloud observation to another. However, since we use common volume observations the total CVE size distribution seen by these instruments for each single observation is per definition the same. The use of the standard Gaussian assumption in the CIPS PMC retrieval has been motivate by lidar studies and model studies (Lumpe et al., 2013). Provided that CIPS makes the correct assumption on the size distribution of the column integrated properties, we seek to understand what size distribution assumptions best represent the local height resolved size distributions seen by OSIRIS.

An instrument that observes scattered radiance is mainly sensitive to particles larger than about 30 nm (Rapp and Thomas, 2006; Merkel et al., 2009). In other words, the behaviour of the curves in Fig. 1 at radii smaller than 30 nm (dashed line) has virtually no effect on the scattered light measurements. If the cloud would have consisted only of particles up 30 nm, certainly these particles up to 30 nm would dominate the optical cloud properties. However, it is commonly accepted that larger particles are needed in order to produce visible clouds. If particles were limited to sizes up to 30 nm, particle number densities needed to produce visible clouds would be unrealistically large, considering available numbers of condensation nuclei. Once there is a significant fraction of larger particles, the strong size-dependence of the scattering lets these particles dominate the optical properties. Hence for all particle populations of visible clouds with commonly expected number densities and size distributions, the contribution of particles smaller than 30 nm to the optical properties becomes largely negligible. To support this statement, we have revisited a broad range of PMC particle populations typically found in literature and calculated the relative contribution to the scattering coefficient from the smaller particles size range. To this end, we have integrated eq. (3) for the example of the wavelength 291.2 nm (one of the seven OSIRIS wavelengths used in the size retrieval) and for a solar scattering angle of 79°. The result is dependent of choice of size distribution. For a Log-normal assumption with a distribution width of 1.5 and mode radius of 30 nm, we find that particles smaller than 30 nm constitute 50 % of the population but contribute to only 2 % of the total scatter. For a Gaussian distribution with a distribution width of 9 nm and mode radius of 30 nm we similarly find that the particles smaller than 30 nm constitute 50 % of the population, but contribute only by 6 % to the total scatter. Using the instrument setup of our current study we are thus more or less blind to the smaller size range, and it would be meaningless to include particles below 30 nm in a comparison of integrated size distribution between the instruments. Studies of the parameter CVE effective radius for the different assumptions are, as previously pointed out, useful to bring particle size estimates that use different size distribution assumptions into a common framework. Using the effective radius provides a measure of how assumptions on the local OSIRIS distribution affect the range of particles that contribute to the bulk mass of ice in the CVE. Finally, we will analyse the parameter IWC for the different assumptions. To reach agreement in IWC for both instruments is of importance since IWC is a desirable property to use for PMC trend studies.

4.2.1. Total size distribution

In this section we evaluate the agreement between the total size distribution, $F_{\mathrm{CVE,\ OSIRIS}}$ and $F_{\mathrm{CVE,\ CIPS}}$ defined in Section 3.2, for different distribution assumptions for OSIRIS while keeping the standard Gaussian assumption for CIPS fixed. We evaluate the agreement by estimating to what extent the total distributions overlap. To this end, we introduce a score S as the ratio of the intersection $\cap$ of CIPS and OSIRIS total size distributions to the average of CIPS and OSIRIS total size distributions.

$$S = \frac{\int_{30nm}^{\infty} \left(F_{\mathrm{CVE,CIPS}} \cap F_{\mathrm{CVE,OSIRIS}}\right) dr}{0.5\left(\int_{30nm}^{\infty} F_{\mathrm{CVE,CIPS}} dr + \int_{30nm}^{\infty} F_{\mathrm{CVE,OSIRIS}} dr\right)} \tag{18}$$

where a score of 1 implies perfect agreement between the total size distributions and 0 implies no agreement. As motivated above, we have restricted the comparison to particles exceeding 30 nm. Note that above the cutoff at 30 nm, we wish to evaluate the whole particle range equally. The score calculation therefore does not take into consideration whether the agreement is better for certain size ranges but merely if the total size range above 30 nm agrees with the other instrument in the CVE. We additionally restrict our comparison to include only those CVE where the reported cloud albedo is brighter than 5 G, based on the discussion in section 4.1.

Fig. 5 shows the score S for various size distribution assumptions for OSIRIS. The highest mean scores are found when a Log-normal assumption with distribution width $\sigma = 1.42$ or an Exponential assumption are used for OSIRIS, resulting in a median score of 0.70 and 0.73, respectively. When either of these two distributions are assumed for OSIRIS local distribution, they give rise to a total distribution that agrees with what is observed simultaneously by CIPS in a large number of the investigated cloud volumes, as indicated by the relatively narrow interquartile ranges combined with high median values. A very narrow distribution assumption for OSIRIS on the other hand, as represented by the Gaussian using a width s of 2 nm, produces a total distribution that in most of the cloud volumes provides poor agreement to the total

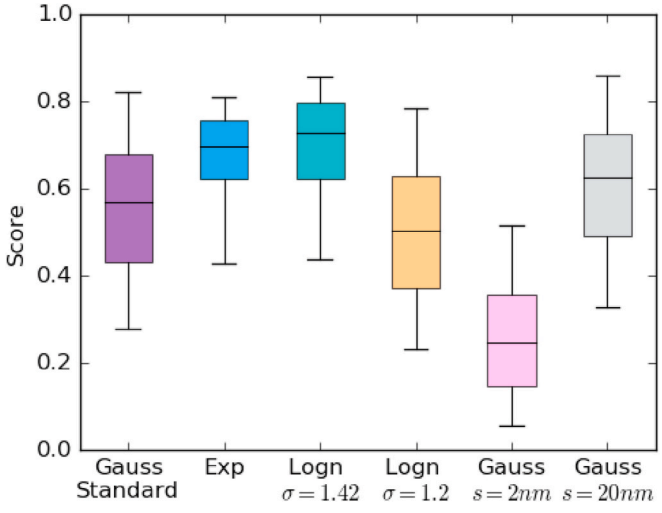

Fig. 5. Boxplot of the score describing the similarity in total size distribution between CIPS and OSIRIS in the CVE for the various size distribution assumptions used for OSIRIS. A score of 1 implies perfect agreement while a score of 0 implies no agreement. The box is drawn from first quartile (Q1) to third quartile (Q3) with a horizontal line drawn in the middle to denote the median. Whiskers above and below the box indicate the 5th and 95th percentiles.

distribution observed by CIPS. A wide Gaussian distribution, as represented by the Gaussian using a width s of 20 nm, provides better agreement to CIPS than the standard Gaussian distribution. The narrow Log-normal assumption with distribution width $\sigma = 1.2$ provides only moderate agreement and fails to replicate the total distribution as observed by CIPS in many cases. In summary these results suggest that to reach consistence in total size distribution, the local size distribution observed by OSIRIS is best represented by a broad distribution, and in particular by a Log-normal distribution with a distribution width $\sigma = 1.42$.

4.2.2. *Effective radius*

The effective radius is an appealing size property to analyse for intercomparisons between instruments or analysis techniques that use different assumptions on the size distribution. By analyzing the effective radius instead of the mode radius, the size retrievals from a Log-normal, Gaussian or Exponential assumption are put in a common framework. The effective radius is also applicable to any other distribution not following a specific mathematical shape like the integrated size distribution in the combined CIPS/OSIRIS CVE. Similarly to previous sections, we adopt the standard Gaussian assumption for CIPS while for OSIRIS the size distribution assumption has been varied. For each assumption applied to OSIRIS, we have calculated the effective radius for each CVE based on the total CVE size distribution. We have then compared that OSIRIS effective radius to the effective radius resulting from the CIPS total CVE size distribution. Fig. 6 shows the results from each distribution assumption for OSIRIS, presented both as scatter plots and histograms. Fig. 6 shows that the broad Log-normal assumption (using $\sigma = 1.42$) provides best agreement with CIPS in CVE effective radius. This indicates that if a broad Log-normal assumption is used for OSIRIS and the standard Gaussian for CIPS, the integrated signal for each instrument will often be comparable and that the range of particles contributing to the bulk ice mass is very similar. This result is in line with the results presented in Bailey et al. (2015b). If the standard Gaussian

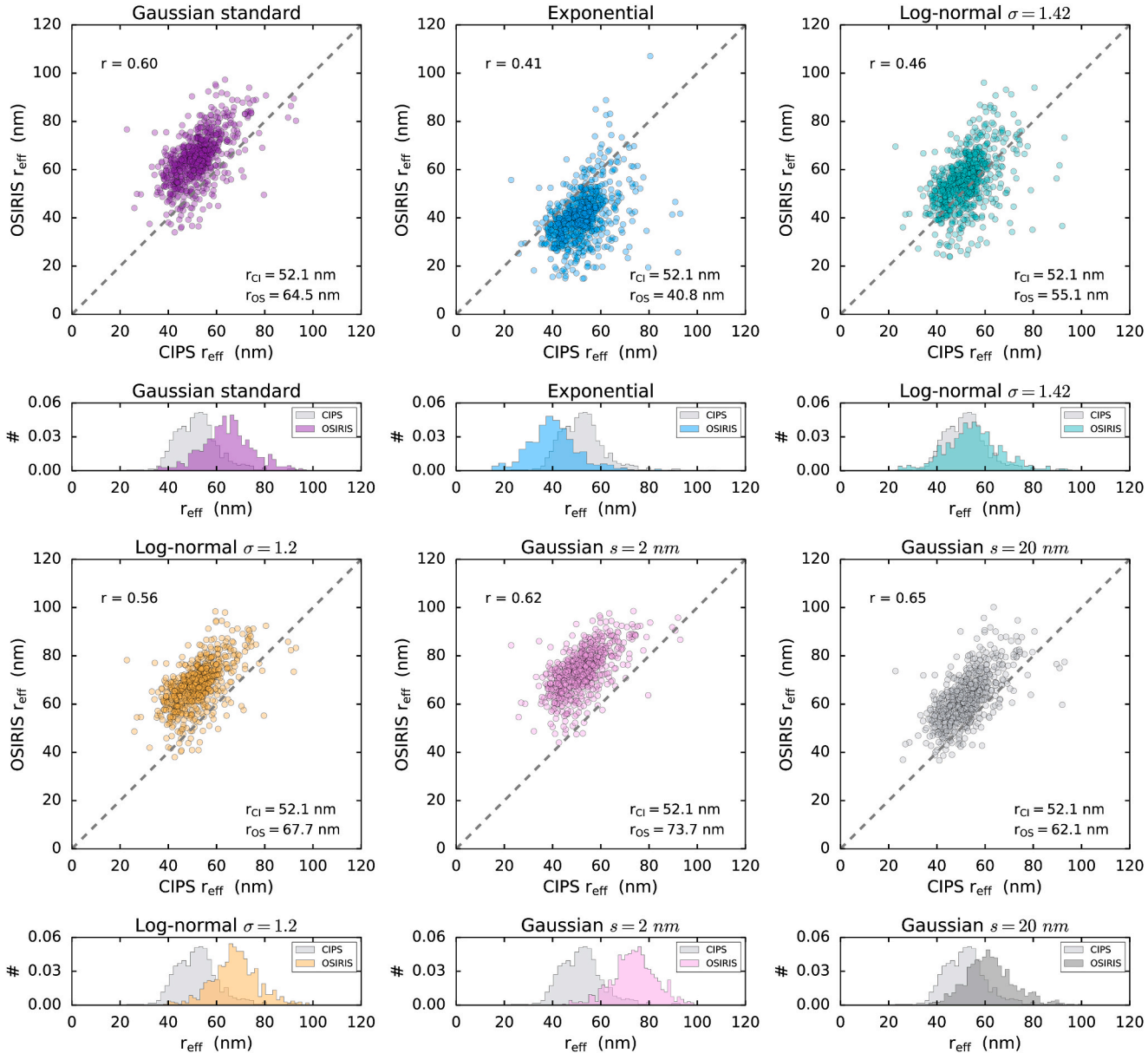

Fig. 6. Comparison of CIPS and OSIRIS retrievals of CVE effective radius for the various size distribution assumptions used for OSIRIS. Panels 1 and 3 show scatter plots of CVE effective radius for NH 2010 - NH2011. The dashed line denotes the one-to-one relationship. For each distribution, the correlation is shown together with the mean of each instrument. Panels 2 and 4 show histograms for the same data. Each histogram is normalized to 1, and the number for bins are 40.

assumption is adopted for OSIRIS, the effective radius is overestimated compared to CIPS. Similarly, if an Exponential assumption is applied to OSIRIS, the effective radius from the integrated distribution is considerably smaller than for CIPS. The narrow Log-normal and narrow Gaussian assumptions for OSIRIS overestimate the effective radius. For the wide Log-normal assumption (and also for the Exponential assumption), the correlation between the instruments is lower than for the standard Gaussian assumption (0.46 in comparison to 0.60). The decrease in correlation is mainly caused by some points where the common volume effective radius is large for CIPS but considerably small for OSIRIS. These points are only a few but exerts enough influence to lower the correlation coefficient. The reason for the small size results for OSIRIS in these particular common volumes is that some grid cells have a very small radius and a very large number density for the Log-normal distribution. Since the CVE effective radius is based on the integrated distribution, this skews the CVE effective radius to a small size for these few points. However, as can be seen by the histogram for the wide Log-normal assumption, the peak of the distributions coincides well for this assumption.

4.2.3. IWC

In Fig. 7, the column ice mass observed by CIPS and OSIRIS in the CVE is compared for the various size assumptions for OSIRIS. All tested distributions for OSIRIS generally lead to IWC that agrees very well with what is observed by CIPS, and the differences between different assumptions are fairly small. This result is expected and is related to the fact that the local ice mass retrieval is fairly insensitive to the assumption on the particle size distribution (Hultgren and Gumbel, 2014). For the standard Gaussian assumption as for a somewhat wider Gaussian assumption, the agreement is very good. However, in cloud volumes containing only small amount of ice, OSIRIS underestimates the amount of ice as compared to CIPS. Improvement in average IWC can be gained if instead a Log-normal assumption with fixed width of 1.42 is used in the calculations for OSIRIS leading to average IWC for OSIRIS of 80.7 g/km^2 and 81.7 g/km^2 for CIPS. When OSIRIS uses a narrow size distribution in the calculations, as represented in the figure by either a Gaussian assumption with fixed width of 2 nm or a Log-normal assumption with fixed width of 1.2, it results in a small underestimate of IWC compared to CIPS, but the correlation is still very good. However, if OSIRIS uses an Exponential distribution in the calculations the agreement in IWC is reduced since a long tail of very large particles carrying much weight is produced.

5. Summary and conclusions

This work focuses on constraining the assumption on the PMC particle size distribution seen by a limb viewing instrument. We use common volume PMC observations from the OSIRIS tomographic dataset and CIPS version 5.20 level 2 dataset from NH PMC seasons 2010 and 2011 from 180 orbits over the latitude range 78° N to 80° N.

One notable finding from this study is that if the commonly used PMC size distribution assumption, namely the standard Gaussian assumption, is adopted to both the column-integrated CIPS instrument and the local distribution seen by the vertically resolving OSIRIS instrument, the mean PMC particle radius reported by OSIRIS is on average 10–15 nm larger than the mean particle size reported by CIPS. If

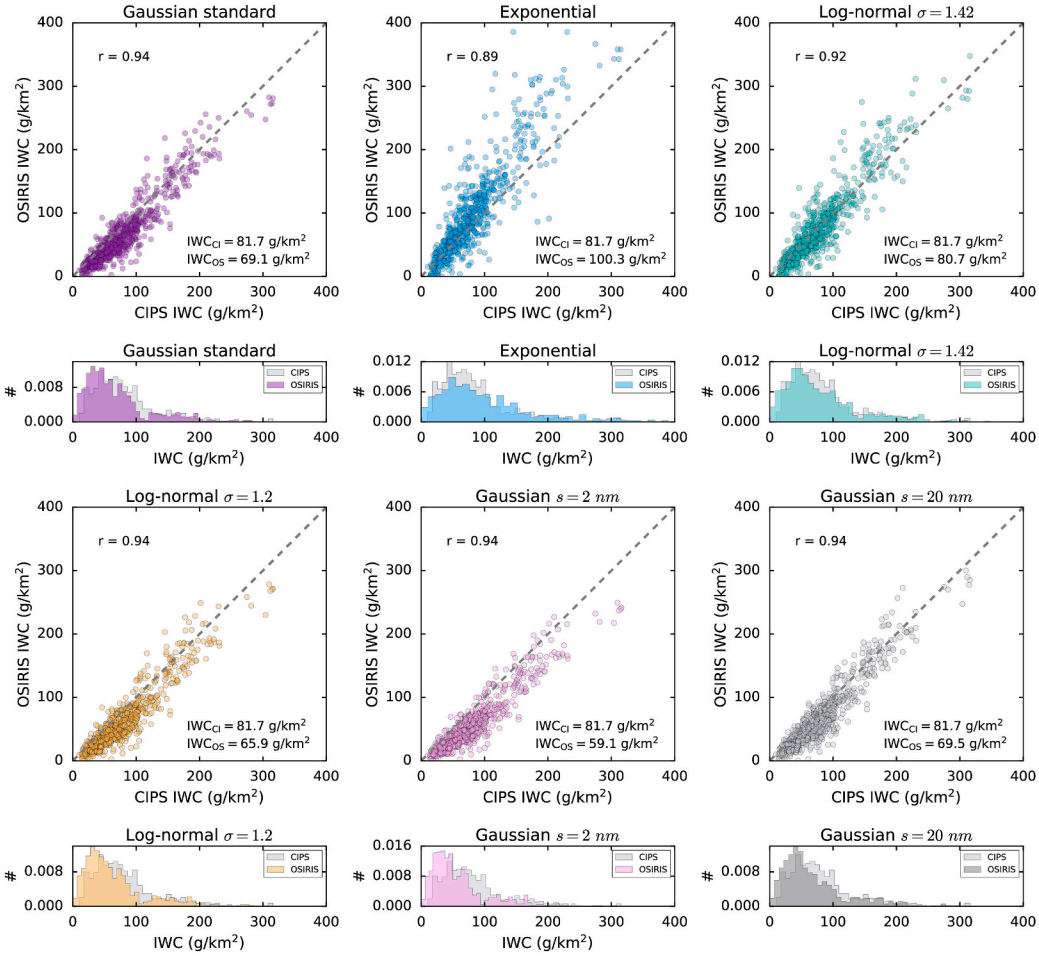

Fig. 7. Comparison of CIPS and OSIRIS retrievals of mean CVE ice water content for the various size distribution assumptions used for OSIRIS. Interpretation of data is same as for Fig. 6.

we assume that the column integrated distribution can be described by a Gaussian distribution, this result implies that the same assumption cannot explain the local distribution seen by the limb instrument. By analyzing the effective radius, the shape of the total size distribution, and the IWC in the common volume element for a large set of assumptions on the size distributions for OSIRIS, we find that the agreement between the instruments can be greatly improved if the local size distribution seen by OSIRIS is assumed to be a broad distribution, and especially a Log-normal distribution with a fixed width around 1.42. This result is in line with Cossart et al. (1999).

We argue that since the instruments observe the same amount of IWC in the common volume, they should also observe the same common volume effective radius. If CIPS assumes a Gaussian size distribution to represent the distribution over the vertical column in each pixel, OSIRIS must assume a broad Log-normal distribution in each vertical grid cell to reach agreement in effective radius in the common volume. If OSIRIS instead adopts narrow size distribution assumptions, the agreement of common volume effective radius to CIPS becomes poor, implying that it is unlikely that the particles in a single vertical OSIRIS grid box are of similar size. Relating back to the discussion in section 4.1, this might be regarded as somewhat unexpected. The interpretation of this result can be understood by first considering the differences in viewing geometry between the instruments. The considerably larger horizontal extent of the OSIRIS grid cells compared to the CIPS pixels likely enables a wider range of gravity waves and gravity wave induced instabilities to simultaneously act on the cloud within each OSIRIS grid cell than each CIPS pixel. We could thus expect that horizontal variations of growth and sublimation of particles cause a larger spread in particle size within the larger OSIRIS grid cell than within the smaller CIPS pixel where gravity waves would affect the ice particles more uniformly. Hence, a broader size distribution assumption could be expected to best represent the range of particles in the OSIRIS observation volume with its larger horizontal extent.

The method outlined in this study shows that it is possible to compare PMC particle sizes in a meaningful way only if we take into account that the viewing geometry inherently implies differences in the local size distributions. Even though the total size distribution for a single observation over common volume element unconditionally is the same for both instruments, the local size distribution seen by OSIRIS needs to be treated different from the column size distribution seen by CIPS. We note that even though our findings suggest that a broad Log-normal assumption is best suited for OSIRIS PMC distribution, we do not expect the same assumption to be best for instruments adopting other viewing geometries with different observation volumes. For future studies it would be of particular interest to extend the conclusions from the current work with comparisons of size distributions to ground based instruments using smaller observation volumes.

Data availability

AIM CIPS data are available at http://lasp.colorado.edu/aim/download-data-L2.php. Odin OSIRIS PMC data for 2010 and 2011 are available at the Bolin Center database (https://bolin.su.se/data/). The supporting information to the manuscript contains the score value for all tested assumptions on the size distribution for OSIRIS.

Author contributions

LB and JG designed the study together. LB was responsible for reprocessing of OSIRIS tomography data and microphysical retrieval used in this study, carried out the analysis and drafted the manuscript. All authors provided critical feedback and contributed to the results discussion and the final version of the manuscript.

Declaration of competing interest

The authors declare that they have no known competing financial interests or personal relationships that could have appeared to influence the work reported in this paper.

Acknowledgements

We thank the two reviewers for useful comments and questions that greatly helped us improve the quality of the manuscript. The authors would also like to thank Cora Randall and Justin Carstens for helpful comments and valuable discussions on the CIPS PMC v5.20 retrieval algorithm. Odin is a Swedish-led satellite funded jointly by Sweden (SNSB), Canada (CSA), France (CNES) and Finland (TEKES). Since 2007, Odin is a third-party mission of the European Space Agency. AIM is supported by NASA Small Explorers contract NAS5-03132. We gratefully acknowledge the efforts of the entire Odin and AIM development, science, and operations teams.

Appendix A. Supplementary data

Supplementary data to this article can be found online at https://doi.org/10.1016/j.jastp.2021.105594.

References

Antonsen, T., Havnes, O., Mann, I., 2017. Estimates of the size distribution of meteoric smoke particles from rocket-borne impact probes. J. Geophys. Res.: Atmosphere 122, 12. https://doi.org/10.1002/2017jd027220, 353–12,365.

Bailey, S., Baumgarden, G., Benze, S., DeLand, M., Gumbel, J., Hervig, M., Karlsson, B., Lumpe, J., Megner, L., Rusch, D., Savigny, C.v., Thomas, G., Thurairajah, B., 2015a. Comparing PMC ice particle sizes observed from ground and space, CIRES, Colorado. https://lpmrcires.colorado.edu/abstracts/#posters.

Bailey, S.M., Thomas, G.E., Hervig, M.E., Lumpe, J.D., Randall, C.E., Carstens, J.N., Thurairajah, B., Rusch, D.W., Russell, J.M., Gordley, L.L., 2015b. Comparing nadir and limb observations of polar mesospheric clouds: the effect of the assumed particle size distribution. J. Atmos. Sol. Terr. Phys. 127, 51–65. https://doi.org/10.1016/j.jastp.2015.02.007.

Bailey, S.M., Thomas, G.E., Rusch, D.W., Merkel, A.W., Jeppesen, C.D., Carstens, J.N., Randall, C.E., McClintock, W.E., Russell, J.M., 2009. Phase functions of polar mesospheric cloud ice as observed by the CIPS instrument on the AIM satellite. J. Atmos. Sol. Terr. Phys. 71, 373–380. https://doi.org/10.1016/j.jastp.2008.09.039.

Bardeen, C.G., Toon, O.B., Jensen, E.J., Hervig, M.E., Randall, C.E., Benze, S., Marsh, D. R., Merkel, A., 2010. Numerical simulations of the three-dimensional distribution of polar mesospheric clouds and comparisons with Cloud Imaging and Particle Size (CIPS) experiment and the Solar Occultation for Ice Experiment (SOFIE) observations. J. Geophys. Res. 115 https://doi.org/10.1029/2009jd012451.

Barth, C.A., Rusch, D.W., Thomas, R.J., Mount, G.H., Rottman, G.J., Thomas, G.E., Sanders, R.W., Lawrence, G.M., 1983. Solar mesosphere explorer: scientific objectives and results. Geophys. Res. Lett. 10, 237–240. https://doi.org/10.1029/gl010i004p00237.

Baumgarten, G., Fiedler, J., Rapp, M., 2010. On microphysical processes of noctilucent clouds (NLC): observations and modeling of mean and width of the particle size-distribution. Atmos. Chem. Phys. 10, 6661–6668. https://doi.org/10.5194/acp-10-6661-2010.

Baumgarten, G., Fritts, D.C., 2014. Quantifying Kelvin-Helmholtz instability dynamics observed in noctilucent clouds: 1. Methods and observations: KHI and turbulence observed IN NLC, #1. J. Geophys. Res.: Atmosphere 119, 9324–9337. https://doi.org/10.1002/2014jd021832.

Broman, L., Benze, S., Gumbel, J., Christensen, O.M., Randall, C.E., 2019. Common volume satellite studies of polar mesospheric clouds with Odin/OSIRIS tomography and AIM/CIPS nadir imaging. Atmos. Chem. Phys. 19, 12455–12475. https://doi.org/10.5194/acp-19-12455-2019.

Carstens, J.N., Bailey, S.M., Lumpe, J.D., Randall, C.E., 2013. Understanding uncertainties in the retrieval of polar mesospheric clouds from the cloud imaging and particle size experiment in the presence of a bright Rayleigh background. J. Atmos. Sol. Terr. Phys. 104, 197–212. https://doi.org/10.1016/j.jastp.2013.08.006.

Chandran, A., Rusch, D.W., Thomas, G.E., Palo, S.E., Baumgarten, G., Jensen, E.J., Merkel, A.W., 2012. Atmospheric gravity wave effects on polar mesospheric clouds: a comparison of numerical simulations from CARMA 2D with AIM observations: CARMA simulation OF CIPS PMC variability. J. Geophys. Res.: Atmosphere 117. https://doi.org/10.1029/2012jd017794.

Christensen, O.M., Benze, S., Eriksson, P., Gumbel, J., Megner, L., Murtagh, D.P., 2016. The relationship between polar mesospheric clouds and their background atmosphere as observed by Odin-SMR and Odin-OSIRIS. Atmos. Chem. Phys. 16, 12587–12600. https://doi.org/10.5194/acp-16-12587-2016.

Cossart, G.v., Fiedler, J., Zahn, U.v., 1999. Size distributions of NLC particles as determined from 3-color observations of NLC by ground-based lidar. Geophys. Res. Lett. 26, 1513–1516. https://doi.org/10.1029/1999gl900226.

Degenstein, D., 1999. Atmosphreic Volume Emission Tomography from a Satellite Platform. Ph.D. thesis.

Degenstein, D.A., Llewellyn, E.J., Lloyd, N.D., 2003. Volume emission rate tomography from a satellite platform. Appl. Optic. 42, 1441. https://doi.org/10.1364/ao.42.001441.

Degenstein, D.A., Llewellyn, E.J., Lloyd, N.D., 2004. Tomographic retrieval of the oxygen infrared atmospheric band with the OSIRIS infrared imager. Can. J. Phys. 82, 501–515. https://doi.org/10.1139/p04-024.

Duft, D., Nachbar, M., Leisner, T., 2019. Unravelling the microphysics of polar mesospheric cloud formation. Atmos. Chem. Phys. 19, 2871–2879. https://doi.org/10.5194/acp-19-2871-2019.

France, J.A., Randall, C.E., Lieberman, R.S., Harvey, V.L., Eckermann, S.D., Siskind, D.E., Lumpe, J.D., Bailey, S.M., Carstens, J.N., Russell, J.M., 2018. Local and remote planetary wave effects on polar mesospheric clouds in the northern hemisphere in 2014. J. Geophys. Res.: Atmosphere 123, 5149–5162. https://doi.org/10.1029/2017jd028224.

Gao, H., Li, L., Bu, L., Zhang, Q., Tang, Y., Wang, Z., 2018. Effect of small-scale gravity waves on polar mesospheric clouds observed from CIPS/AIM. J. Geophys. Res.: Space Phys. 123, 4026–4045. https://doi.org/10.1029/2017ja024855.

Gumbel, J., Megner, L., 2009. Charged meteoric smoke as ice nuclei in the mesosphere: Part 1-A review of basic concepts. J. Atmos. Sol. Terr. Phys. 71, 1225–1235. https://doi.org/10.1016/j.jastp.2009.04.012.

Hervig, M.E., Deaver, L.E., Bardeen, C.G., Russell, J.M., Bailey, S.M., Gordley, L.L., 2012. The content and composition of meteoric smoke in mesospheric ice particles from SOFIE observations. J. Atmos. Sol. Terr. Phys. 84, 1–6. https://doi.org/10.1016/j.jastp.2012.04.005.

Hervig, M.E., Gordley, L.L., Russell, J.M., Bailey, S.M., 2009. SOFIE PMC observations during the northern summer of 2007. J. Atmos. Sol. Terr. Phys. 71, 331–339. https://doi.org/10.1016/j.jastp.2008.08.010.

Hultgren, K., Gumbel, J., 2014. Tomographic and spectral views on the lifecycle of polar mesospheric clouds from Odin/OSIRIS. J. Geophys. Res.: Atmosphere 119, 14. https://doi.org/10.1002/2014jd022435, 129–14,143.

Hultgren, K., Gumbel, J., Degenstein, D., Bourassa, A., Lloyd, N., Stegman, J., 2013. First simultaneous retrievals of horizontal and vertical structures of Polar Mesospheric Clouds from Odin/OSIRIS tomography. J. Atmos. Sol. Terr. Phys. 104, 213–223. https://doi.org/10.1016/j.jastp.2013.06.013.

Karlsson, B., Gumbel, J., 2005. Challenges in the limb retrieval of noctilucent cloud properties from Odin/OSIRIS. Adv. Space Res. 36, 935–942. https://doi.org/10.1016/j.asr.2005.04.074.

Kiliani, J., Baumgarten, G., Lübken, F.J., Berger, U., Hoffmann, P., 2013. Temporal and spatial characteristics of the formation of strong noctilucent clouds. J. Atmos. Sol. Terr. Phys. 104, 151–166. https://doi.org/10.1016/j.jastp.2013.01.005.

Llewellyn, E.J., Lloyd, N.D., Degenstein, D.A., Gattinger, R.L., Petelina, S.V., Bourassa, A. E., Wiensz, J.T., Ivanov, E.V., McDade, I.C., Solheim, B.H., McConnell, J.C., Haley, C. S., Savigny, C.v., Sioris, C.E., McLinden, C.A., Griffioen, E., Kaminski, J., Evans, W.F., Puckrin, E., Strong, K., Wehrle, V., Hum, R.H., Kendall, D.J., Matsushita, J., Murtagh, D.P., Brohede, S., Stegman, J., Witt, G., Barnes, G., Payne, W.F., Piché, L., Smith, K., Warshaw, G., Deslauniers, D.L., Marchand, P., Richardson, E.H., King, R. A., Wevers, I., McCreath, W., Kyrölä, E., Oikarinen, L., Leppelmeier, G.W., Auvinen, H., Mégie, G., Hauchecorne, A., Lefẽvre, F., Nöe, J.d.L., Ricaud, P., Frisk, U., Sjoberg, F., Schéele, F.v., Nordh, L., 2004. The OSIRIS instrument on the Odin spacecraft. Can. J. Phys. 82, 411–422. https://doi.org/10.1139/p04-005.

Lloyd, N.D., Llewellyn, E.J., 1989. Deconvolution of blurred images using photon counting statistics and maximum probability. Can. J. Phys. 67, 89–94. https://doi.org/10.1139/p89-013.

Lumpe, J.D., Bailey, S.M., Carstens, J.N., Randall, C.E., Rusch, D.W., Thomas, G.E., Nielsen, K., Jeppesen, C., McClintock, W.E., Merkel, A.W., Riesberg, L., Templeman, B., Baumgarten, G., Russell, J.M., 2013. Retrieval of polar mesospheric cloud properties from CIPS: algorithm description, error analysis and cloud detection sensitivity. J. Atmos. Sol. Terr. Phys. 104, 167–196. https://doi.org/10.1016/j.jastp.2013.06.007.

McClintock, W.E., Rusch, D.W., Thomas, G.E., Merkel, A.W., Lankton, M.R., Drake, V.A., Bailey, S.M., Russell, J.M., 2009. The cloud imaging and particle size experiment on the Aeronomy of Ice in the mesosphere mission: instrument concept, design, calibration, and on-orbit performance. J. Atmos. Sol. Terr. Phys. 71, 340–355. https://doi.org/10.1016/j.jastp.2008.10.011.

Megner, L., 2011. Minimal impact of condensation nuclei characteristics on observable Mesospheric ice properties. J. Atmos. Sol. Terr. Phys. 73, 2184–2191. https://doi.org/10.1016/j.jastp.2010.08.006.

Megner, L., Christensen, O.M., Karlsson, B., Benze, S., Fomichev, V.I., 2016. Comparison of retrieved noctilucent cloud particle properties from Odin tomography scans and model simulations. Atmos. Chem. Phys. 16, 15135–15146. https://doi.org/10.5194/acp-16-15135-2016.

Merkel, A.W., Marsh, D.R., Gettelman, A., Jensen, E.J., 2009. On the relationship of polar mesospheric cloud ice water content, particle radius and mesospheric temperature and its use in multi-dimensional models. Atmos. Chem. Phys. 9, 8889–8901. https://doi.org/10.5194/acp-9-8889-2009.

Mishchenko, M.I., Travis, L.D., 1998. Capabilities and limitations of a current FORTRAN implementation of the T-matrix method for randomly oriented, rotationally symmetric scatterers. J. Quant. Spectrosc. Radiat. Transf. 60, 309–324. https://doi.org/10.1016/s0022-4073(98)00008-9.

Murtagh, D., Frisk, U., Merino, F., Ridal, M., Jonsson, A., Stegman, J., Witt, G., Eriksson, P., Jiménez, C., Megie, G., Noë, J.d.l., Ricaud, P., Baron, P., Pardo, J.R., Hauchcorne, A., Llewellyn, E.J., Degenstein, D.A., Gattinger, R.L., Lloyd, N.D., Evans, W.F., McDade, I.C., Haley, C.S., Sioris, C., Savigny, C.v., Solheim, B.H., McConnell, J.C., Strong, K., Richardson, E.H., Leppelmeier, G.W., Kyrölä, E., Auvinen, H., Oikarinen, L., 2002. An overview of the Odin atmospheric mission. Can. J. Phys. 80, 309–319. https://doi.org/10.1139/p01-157.

Rapp, M., Thomas, G.E., 2006. Modeling the microphysics of mesospheric ice particles: assessment of current capabilities and basic sensitivities. J. Atmos. Sol. Terr. Phys. 68, 715–744. https://doi.org/10.1016/j.jastp.2005.10.015.

Robert, C.E., Savigny, C.v., Burrows, J.P., Baumgarten, G., 2009. Climatology of noctilucent cloud radii and occurrence frequency using SCIAMACHY. J. Atmos. Sol. Terr. Phys. 71, 408–423. https://doi.org/10.1016/j.jastp.2008.10.015.

Rusch, D., Thomas, G., Merkel, A., Olivero, J., Chandran, A., Lumpe, J., Carstans, J., Randall, C., Bailey, S., Russell, J., 2017. Large ice particles associated with small ice water content observed by AIM CIPS imagery of polar mesospheric clouds: evidence for microphysical coupling with small-scale dynamics. J. Atmos. Sol. Terr. Phys. 162, 97–105. https://doi.org/10.1016/j.jastp.2016.04.018.

Rusch, D.W., Thomas, G.E., McClintock, W., Merkel, A.W., Bailey, S.M., Russell, J.M., Randall, C.E., Jeppesen, C., Callan, M., 2009. The cloud imaging and particle size experiment on the aeronomy of ice in the mesosphere mission: cloud morphology for the northern 2007 season. J. Atmos. Sol. Terr. Phys. 71, 356–364. https://doi.org/10.1016/j.jastp.2008.11.005.

Russell, J.M., Bailey, S.M., Gordley, L.L., Rusch, D.W., Horányi, M., Hervig, M.E., Thomas, G.E., Randall, C.E., Siskind, D.E., Stevens, M.H., Summers, M.E., Taylor, M. J., Englert, C.R., Espy, P.J., McClintock, W.E., Merkel, A.W., 2009. The Aeronomy of Ice in the Mesosphere (AIM) mission: overview and early science results. J. Atmos. Sol. Terr. Phys. 71, 289–299. https://doi.org/10.1016/j.jastp.2008.08.011.

Savigny, C.v., Burrows, J.P., 2007. Latitudinal variation of NLC particle radii derived from northern hemisphere SCIAMACHY/Envisat limb measurements. Adv. Space Res. 40, 765–771. https://doi.org/10.1016/j.asr.2006.12.032.

Savigny, C.v., Petelina, S.V., Karlsson, B., Llewellyn, E.J., Degenstein, D.A., Lloyd, N.D., Burrows, J.P., 2005. Vertical variation of NLC particle sizes retrieved from Odin/OSIRIS limb scattering observations. Geophys. Res. Lett. 32 n/a–n/a. doi:10.1029/2004gl021982.

Thomas, G.E., McKay, C.P., 1985. On the mean particle size and water content of polar mesospheric clouds. Planet. Space Sci. 33, 1209–1224. https://doi.org/10.1016/0032-0633(85)90077-7.

Thurairajah, B., Bailey, S.M., Nielsen, K., Randall, C.E., Lumpe, J.D., Taylor, M.J., Russell, J.M., 2013. Morphology of polar mesospheric clouds as seen from space. J. Atmos. Sol. Terr. Phys. 104, 234–243. https://doi.org/10.1016/j.jastp.2012.09.009.

Thurairajah, B., Sato, K., Yue, J., Nakamura, T., Kohma, M., Bailey, S.M., Russell, J.M., 2017. Simultaneous observation of gravity waves at PMC altitude from AIM/CIPS experiment and PANSY radar over Syowa (69°S, 39°E). J. Atmos. Sol. Terr. Phys. 164, 324–331. https://doi.org/10.1016/j.jastp.2017.10.006.

Tozer, W.F., Beeson, D.E., 1974. Optical model of noctilucent clouds based on polarimetric measurements from two sounding rocket campaigns. J. Geophys. Res. 79, 5607–5612. https://doi.org/10.1029/jc079i036p05607.

Wilms, H., Rapp, M., Kirsch, A., 2016. Nucleation of mesospheric cloud particles: sensitivities and limits. J. Geophys. Res.: Space Phys. 121, 2621–2644. https://doi.org/10.1002/2015ja021764.

Witt, G., 1960. A note to the paper by G. Witt, "Polarization of light from noctilucent clouds". J. Geophys. Res. 65, 2199–2200. https://doi.org/10.1029/jz065i007p02199.

Wyser, K., 1998. The effective radius in ice clouds. J. Clim. 11, 1793–1802. https://doi.org/10.1175/1520-0442(1998)011<1793:teriic>2.0.co;2.

Zahn, U.v., Berger, U., 2003. Persistent ice cloud in the midsummer upper mesosphere at high latitudes: three-dimensional modeling and cloud interactions with ambient water vapor. J. Geophys. Res.: Atmosphere (1984–2012), 108. https://doi.org/10.1029/2002jd002409.